

See discussions, stats, and author profiles for this publication at: <https://www.researchgate.net/publication/364334484>

Auto-MyIn: Automatic diagnosis of myocardial infarction via multiple GLCMs, CNNs, and SVMs

Article in *Biomedical Signal Processing and Control* · February 2023

DOI: 10.1016/j.bspc.2022.104273

CITATIONS

35

READS

281

2 authors:



[Omneya Attallah](#)

Arab Academy for Science, Technology, and Maritime Transport

82 PUBLICATIONS 2,311 CITATIONS

[SEE PROFILE](#)



[Dina A. Ragab](#)

Arab Academy for Science, Technology, and Maritime Transport

14 PUBLICATIONS 941 CITATIONS

[SEE PROFILE](#)

Auto-MyIn: Automatic Diagnosis of Myocardial Infarction via Multiple GLCMs, CNNs, and SVMs

Omneya Attallah ^{1*}, and Dina A. Ragab¹

¹ Electronics & Communications Engineering Department, Arab Academy for Science, Technology, and Maritime Transport (AASTMT), Alexandria 1029, Egypt.

* Correspondence: o.attallah@aast.edu

Abstract: This paper proposes an automated diagnostic tool namely, Auto-MyIn, for diagnosing myocardial infarction (MI) using multiple convolutional neural networks (CNN). Rather than utilizing the spatial information of the original delayed-enhancement magnetic resonance (DE-MRI) images, Auto-MyIn uses the textural information obtained by applying grey level co-occurrence matrix (GLCM) of four different grey levels to train the three CNNs (ResNet-18, DarkNet-19, and SqueezeNet). First, ~~images~~the images generated from each GLCM grey level are used to train each CNN individually. Next, for each GLCM grey level, the textural-based deep features extracted from the three CNNs are concatenated and used to train several support vector machine (SVM) classifiers. Finally, Auto-MyIn fuses textural-based deep features of the four GLCM grey levels using principal component analysis (PCA). The results of Auto-MyIn indicated that fusing the textural-based deep features of each level of GLCM is better than the end-to-end deep learning classification of the three CNNs trained with each grey level of GLCM images. Furthermore, it showed that fusing textural-based deep features of the four grey levels of the GLCM using PCA has further improvement on diagnostic accuracy. Moreover, the results prove that using textural information is superior to using spatial information of the original DE-MRI images. In addition, the results of Auto-MyIn when compared with other related studies demonstrated its competitive ability. Moreover, the performance of Auto-MyIn shows an accuracy of 0.984, a sensitivity of 0.992, specificity of 0.968, and precision of 0.967, which indicate that it is a reliable tool, therefore it could be employed to help in the clinical decision making and facilitate the diagnostic process of MI thus avoiding the limitations of manual diagnosis.

Keywords: Cardiovascular (CV) Diseases; Myocardial Infarction (MI) Diagnosis; Artificial Intelligence (AI), Deep Learning, Convolutional Neural Network (CNN), Grey level Co-occurrence Matrix(GLCM), **Support Vector Machine (SVM)**.

1. Introduction

Cardiovascular diseases are the foremost reason for death globally. ~~Annually~~Annually, around 17.3 million deaths occur due to cardiovascular diseases [1]. This amount of deaths are predicted to rise and exceed 23.6 million by 2030 [2]. Almost 85% of these deaths are because of heart attacks and strokes [3]. Around 647,000 deaths happen due to heart attacks in the USA only. Myocardial infarction (MI) which is popularly known as “heart attack” is a threatening cardiovascular condition that occurs due to a destruction in the myocardium region because of an obstacle in the blood flow in one or more of the coronary arteries and this leads to damage in the ~~of~~range of the heart [4],[5]. This obstruction may be created due to high cholesterol levels, excess fats, and cellular waste products [6]. In the initial phase of MI, individuals frequently reveal indications such as chest rigidity and chest pain, however, some individuals still have no clear signs, which makes it challenging to cure them in time, hence endangering life [7]. Thus, exactly how to attain the primary diagnosis of MI has considerable clinical ~~importance~~importance and has attracted many scholars [8]. Every 43 seconds an individual experiences an MI in the USA [9]. Even in developed countries, the number of MI cases is still increasing tremendously [10], [11]. Such as India, an individual dies from MI every 33 seconds and around 2 million persons suffer from a heart attack annually. The majority of these cases are

young individuals [4]. Therefore, early and precise detection and diagnosis of MI are essential for lowering the death rate due to MI.

Several imaging techniques are used to diagnose cardiovascular diseases such as Echocardiography [12], Cardiac Computed Tomography, Cardiac Nuclear Imaging, and Cardiac Magnetic Resonance Imaging (MRI). Among these methods, cardiac MRI shows an essential role in the early diagnosis, prediction, and detection of arrhythmia in assessing the different phases of a-MMI [13]. It has several advantages over other imaging methods [13], [14],[15]. Cardiac MRI offers crucial knowledge about cardiovascular diagnosis via allowing numerical evaluation of useful features such as the volume of the left and right ventricles, myocardium thickness, and ejection fraction (EF) [1]. The spatiotemporal high resolution and great contrast resolution of the MRI image facilitate envisaging tissue features, which may improve diagnostic accuracy compared to other imaging modalities used in clinical practice. Also, cardiac MRI may be easily reproduced compared to other imaging techniques utilized in clinical practice. Moreover, it is considered a time saver method and the patient will not expose to harmful radiation [14]. Besides, it has the prospective to decrease any further image acquisition procedures that might be needed compared to other scanning methods [14]. Among cardiac MRI techniques; delayed-enhancement MRI (DE-MRI) is believed to be the non-invasive gold criterion for evaluating and diagnosing MI conditions, diseases in the coronary artery[16],[17], and distinguishing between ischemic from non-ischemic myocardial illness [18]. In DE-MRI, an MRI is executed a few minutes after injecting a contrast agent. This agent enhances the quality of the image and facilitates the recognition of damaged areas. DE-MRI procedure can also evaluate the size of MI, and by knowing this information, doctors can be able to evaluate feasible tissues following an injury. However, cardiopathy diagnosis ~~from~~by DE-MRI is a very complex procedure [1]. This complexity makes the detection, diagnosis, and classification of such images a challenging task.

To resolve these problems, artificial intelligence (AI) techniques may be used to help the doctor as a second diagnostic opinion. In the last decade, there have been ~~huge~~large successes in using AI techniques such as machine and deep learning [19]. Such methods have been widely used in many medical related problems such as lung illness [20], breast cancer [21],[22] , heart diseases [23],[24],[25],[26], brain disorders [27],[28], and eye diseases [29]. Deep learning approaches including convolution neural networks (CNN) automatically realize and obtain features from images via deep networks, distinct from the attainment of classical handcrafted ~~features~~feature extraction methods and professional experience [8]. Recently, there has been a growing interest in AI techniques in cardiovascular (CV) medicine [30]. AI technology can help in facilitating the diagnosis procedure of CV diseases such as MI. AI can also enable to enhance the realizing of disease statuses and create a personalized methodology to CV care [14],[31]. Several research articles have been recently presented to classify CV diseases using AI techniques [8],[32],[15]. Larroza et al. [33] proposed a fully automated AI method to diagnose MI from cardiac MRI images. The authors in [34] proposed an automatic system for diagnosing MI disease from cardiac MRI. They first extracted significant features using several classical feature extraction methods and then applied a feature selection procedure based on a support vector machine (SVM) classifier to select the most significant features. The authors in [13] proposed a framework for classifying MI from DE-MRI images. Initially, the damaged regions were segmented using a fuzzy-c-means clustering method. Afterwards, features were extracted using morphological features. Finally, classical artificial neural network (ANN) was constructed for classification and achieved an accuracy of 99.9%.

Khened et al. in [35] introduced a method for classifying four CV diseases including dilated cardiomyopathy, MI, abnormal RV, and hypertrophic cardiomyopathy. ~~First~~First, DenseNet CNN was used for the segmentation process. Afterward, some cardiac features were measured from the segmented images. Finally, these features were used to construct an RF classifier achieving an accuracy of 90%. The authors in [36] used several U-Net to segment cardiac MRI images. Then, classical cardiac features were measured from these segmented images. Lastly, an ensemble of classical ANNs models was created to classify four CV diseases achieving an accuracy of 92%. These papers suffer from using only one type of classical cardiac feature to construct the classification model. ~~Also~~Moreover, the authors used ~~classical~~the classical ANN for performing classification. This technique suffered from the small size of the dataset used for classification. Classification models constructed with small datasets are not adequate to accomplish diagnosis in complicated clinical settings. Moreover, the authors employed only one type of CNN for classification. ~~Also~~Moreover, they used only spatial information for performing the classification procedure. The authors in [37] proposed an automatic approach for MI diagnosis. It is based on R-CNN for segmenting images, then

auto-encoder deep learning method which mixes static and optical flow features extracted from these segmented images and reduces the dimension of the features entering an SVM classifier. The accuracy attained was 87.6%, which is quite low for medical applications. Later On, the authors in [1] proposed a pipeline for automatic segmentation and classification of cardiovascular diseases such as myocardial infarction, dilated cardiomyopathy, hypertrophic cardiomyopathy, and abnormal right ventricle from Cardiac MRI. They first employed deep CNNs to segment the region of interest (ROI) based on the you only look once (YOLO) detector. Next, the author sampled uniform 3D point clouds at random and then used these points to train another CNN for the classification process. The authors in [38] developed an automated method to detect and localize the size and position of MI in DE-MRI images. They used [jellysJollys](#) algorithm for segmenting the image, then extracted significant features using [opticalthe optical](#) flow method. Finally, classification was made using an SVM classifier and an accuracy of 93.4% was obtained.

Later, Shi et al. in [39] presented a two-stage approach that combines clinical information with features extracted using CNN from DE-MRI images to diagnose MI via Random Forest (RF) classifier. In the same year, Lourenco et al. in [40] proposed a pipeline for the automatic prediction of MI disease. The authors first segmented the DE-MRI images using two U-CNNs and then constructed a CNN to predict MI cases using both clinical information and data from DE-MRI. The classification accuracy achieved was 95%. Sharma et al. in [41] introduced a novel CNN architecture called Stacked Multimodal (SM2N2) [CNNCNN](#), which combines slices of DE-MRI with clinical data to perform MI diagnosis. The classification accuracy obtained was 90%. The authors in [42] proposed a framework for the automatic classification of MI from DE-MRI. They first used U-Net to segment the LV from the image. Then, utilized radiomics for feature extraction. Afterward, they combine these features with clinical data. Finally, classification is performed using four individual classifiers. The peak accuracy achieved was 93% using the RF classifier. The authors [43] constructed a novel U-Net architecture based on the inclusion and classification of prior information to segment and classify left ventricle disease from DE-MRI, reaching an accuracy of 98%. The study [44] proposed cascaded segmentation methods based on morphological operation and ensemble lightweight CNNs reaching a dice coefficient of 0.77. A summary of related studies along with their limitations is shown in table 1.

Table 1 Recent related studies are summarized along with their limitations

Article	Method	Accuracy	Limitations
[33]	<ul style="list-style-type: none"> Five textural analysis features SVM 	77.8%	<ul style="list-style-type: none"> Dataset was small. Used only textual features. Employed classical ML methodsmethod. Did not use DL methodsmethod. Low accuracy
[34]	<ul style="list-style-type: none"> Several classical feature extraction methods. Feature selection SVM 	89.9%	<ul style="list-style-type: none"> Used only handcrafted feature extraction methods. Employed classical ML methodsmethod. Did not use DL methods
[13]	<ul style="list-style-type: none"> Fuzzy-c-means clustering for segmentation. Morphological features. ANN 	99.9%	<ul style="list-style-type: none"> Used only handcrafted feature extraction methods. Employed classical ML methodsmethod. Did not use DL methods
[35]	<ul style="list-style-type: none"> DenseNet CNN for segmentation Some cardiac features RF 	90%	<ul style="list-style-type: none"> Only one type of CNN was used. Only a few handcrafted cardiac features were extracted. DL features were not extracted.
[36]	<ul style="list-style-type: none"> Several U-Net for segmentation. Classical cardiac features were measured An ensemble of classical ANNs 	92%	<ul style="list-style-type: none"> Small size of the dataset Employed only one type of CNN for classification. Used only spatial features for classification
[37]	<ul style="list-style-type: none"> R-CNN for segmentation Optical flow features Static features Auto-encoder SVM 	87.6%	<ul style="list-style-type: none"> Only handcrafted features were extracted. DL features were not extracted. Low accuracy
[1]	<ul style="list-style-type: none"> Two deep CNNs based on YOLO for segmentation. Sampled uniform 3D point clouds at random. 	92%	<ul style="list-style-type: none"> Employed only one type of CNN for classification. Used only spatial features for classification

	• Another CNN for the classification		
[38]	<ul style="list-style-type: none"> Jollys algorithm for segmenting Optical flow SVM 	93.4%	<ul style="list-style-type: none"> Used only classical feature extractors. Did not employ any DL approach. The method was based on one type of feature.
[39]	<ul style="list-style-type: none"> Clinical information DL features were extracted via CNN. RF 	95%	<ul style="list-style-type: none"> Extracted only spatial features. Used only one type of feature extracted from either one CNN.
[40]	<ul style="list-style-type: none"> Two U-Nets for segmentation A CNN combines clinical information and data from DE-MRI 	95%	<ul style="list-style-type: none"> Extracted only spatial features. Used only one type of feature extracted from one CNN
[41]	<ul style="list-style-type: none"> SM2N2 	90%	<ul style="list-style-type: none"> Extracted only spatial features. Used only one type of feature extracted from one CNN.
[42]	<ul style="list-style-type: none"> U-Net for segmentation Radiomics plus clinical data for feature extraction. RF 	93%	<ul style="list-style-type: none"> Extracted only spatial features. Used only one type of feature extracted from the classical feature extraction method.
[43]	<ul style="list-style-type: none"> A modified version of U-Net based on the inclusion and classification information 	98%	<ul style="list-style-type: none"> Extracted only spatial features. Used only one type of feature extracted from the classical feature extraction method.

Despite the promising results of the previous studies, they experience some limitations. First, most of them employed distinct DL models to either do classification or feature extraction. However, employing ensemble DL models to carry out classification or extract features may enhance diagnostic performance [45–48]. Second, to achieve classification, they solely extracted spatial information from DE-MRI images. Only one sort of feature was employed, either from a CNN or a traditional feature extraction technique. But incorporating ~~multi-dimensional~~ multidimensional features can result in more accurate diagnostic outcomes [48–51]. Most of the earlier work has not examined this combined approach. Additionally, they all used segmentation techniques before classification, which makes the final model more difficult. Finally, the majority of them combined clinical data to do classification, increasing the computing burden of the diagnostic step. All these limitations have motivated the authors to propose an automated tool called Auto-MyIn to diagnose MI using DE-MRI images using ensemble CNNs of different architectures to extract features from not only one CNN. Additionally, Auto-MyIn is not only based on the spatial information to learn the CNN models but depends on the textural information as well. The inclusion of textural and deep elements has made it possible to accurately diagnose a number of diseases [48]. This is done by applying GLCM textural-based analysis on DE-MRI images and then using the output GLCM analysis as ~~inputs~~input to the CNN models. Furthermore, Auto-MyIn extracts deep features of the distinct CNN architectures and fuses them using principal component analysis. Also, the proposed tool does not use a segmentation step prior to classification. It also does not use ~~the clinical~~clinical information.

The authors previous studies [21,22,52,53] used the original images or enhanced segmented version of the images to either train the deep learning models or extract handcrafted features to train machine learning classifiers. However, this study uses GLCM method to characterize texture information from the original images. This is performed by studying the spatial relationships between ~~grey~~the grey levels included in an image and determining the frequency with which a collection of grey levels appears together in an image ~~at in~~ a certain direction. Afterwards, scaled images are generated from the GLCM with different number of grey. These images are used as inputs to train the deep learning models of the Auto-MyIn instead of the original images. This procedure allows the deep learning models of Auto-MyIn to benefit from the texture information included in the ~~image~~image, not only spatial information like previous methods.

The paper is organized as follows: Section 2 introduces the methodology of the paper, Section 3 shows the experimental setup, and Section 4 shows the computed results of the technique. A discussion of the suggested technique is presented in section 5 and finally, the work is concluded in section 6

2. Materials and Methods

2.1. Emidec Dataset Description

The Emidec dataset [3] is a new DE-MRI dataset containing images of MI. The dataset was presented in the automatic Evaluation of Myocardial Infarction from Delayed-Enhancement Cardiac MRI (Emidec) challenge arranged in concurrence with the STACOM workshop during the MICCAI conference in 2020. This dataset contains 150 patients involving DE-MRI images as well as clinical physiology information for these patients. The data for the initial 100 patients are publicly available online for [the clinical](#) patient information, DE-MRI exams, and ground truth. The objective of this dataset is to diagnose patients with MI. [The](#) number of normal patients is 33 and patients with MI is 67 analogous approximately to [truly true](#) life scenarios in an MRI department. The medical data comprises 12 parameters. These parameter values are either oat, Boolean, or categorical. Regarding DE-MRI exams, each patient has on average 7 slices. Manual segmentations were done using the QIR software conducted by two specialists. Samples of DE-MRI images for normal and pathology cases are shown in Figure 1.

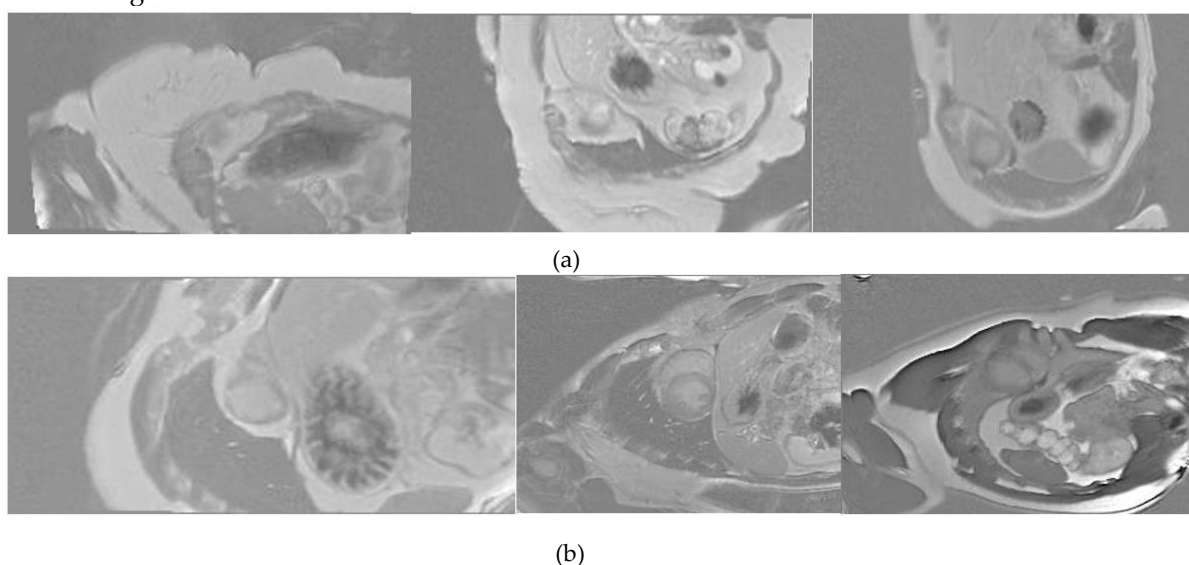


Figure 1. Samples of Emidec dataset; (a) normal heart [images](#); (b) pathological heart images.

2.2. Deep Learning Approaches

DL is the latest branch of machine learning techniques. DL methods arose to solve the limitations of the conventional shallow artificial neural networks ([ANN](#)), which did not account for the underlying spatial information that exists in the image. ANN only considers [structures](#) of activation neurons as they are found in a predetermined order of the training set of data [54]. DL techniques have been widely utilized in many fields including the medical area because of their extreme capacity of avoiding the limitation of standard ANN and other CML methods [55]. ANNs based on DL have several structures; among them, the convolution neural [networks](#) (CNN) is the most commonly used architecture for medical diagnosis from images and videos [56],[57], [22]. Therefore, four state-of-the-art CNNs are utilized in this article to construct Auto-MyIn.

The learning process of a CNN endures some difficulties because of the overfitting and convergence issues, which require permeant adjustments in the parameters or structure of the CNN to ensure that all layers are trained at the same pace. Transfer learning (TL) offers a resolution to such difficulties. TL reutilizes the convolutional neural networks (CNNs) that were previously learned [with on](#) massive datasets such as ImageNet on other comparable problems but with a smaller amount of photos [58] similar to the DSF dataset utilized in this paper. As the pre-trained CNN has already demonstrated image attributes from a [huge large](#) amount of diverse images through TL, it has been shown to improve the accuracy of classification [59],[60],[61]. Thus, TL is utilized with three [pre-](#)

~~trained~~ pretrained CNNs such as; ResNet-18, DarkNet-19, and SqueezeNet architectures instead of creating CNNs from scratch to diagnose single and multiple diseases from face images.

ResNet-18

In ~~year~~the year 2015, He et al. introduced the ResNet which stands for residual ~~networks~~network. ResNet has some common architectures, among them ResNet-18 architecture, which consists of 72-layer architecture with 18 deep layers. The architecture of this network consists of large amounts of convolutional layers to function efficiently. On the other hand, adding multiple deep layers to a network often results in a degradation of the output [62]. The architecture of ResNet-18 is shown in Table 2.

Table 2 The architecture of the ResNet-18 CNN.

Layer Name	Output Size	ResNet-18
Input Layer		$224 \times 224 \times 3$
conv1	$112 \times 112 \times 64$	Filter size = 7×7 Number of filters = 64 Stride = 2 Padding = 3
pool1	$56 \times 56 \times 64$	Pool size = 3×3 Stride = 2
conv2_x	$56 \times 56 \times 64$	$\begin{bmatrix} 3 \times 3, & 64 \\ 3 \times 3, & 64 \end{bmatrix} \times 2$
conv3_x	$28 \times 28 \times 128$	$\begin{bmatrix} 3 \times 3, & 128 \\ 3 \times 3, & 128 \end{bmatrix} \times 2$
conv4_x	$14 \times 14 \times 256$	$\begin{bmatrix} 3 \times 3, & 256 \\ 3 \times 3, & 256 \end{bmatrix} \times 2$
conv5_x	$7 \times 7 \times 512$	$\begin{bmatrix} 3 \times 3, & 512 \\ 3 \times 3, & 512 \end{bmatrix} \times 2$
Average pooling		Pool size = 7×7 Stride = 7
		$1 \times 1 \times 512$
Fully connected (fc)		2 (512×2)

DarkNet-19

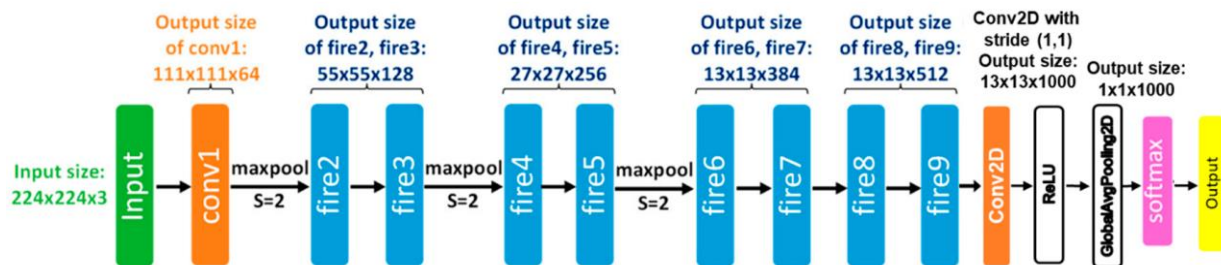
DarkNet-19 is a new classification model to be used as the base of YOLOv2. It is similar to the VGG models. It uses mostly 3×3 filters and ~~double~~doubles the number of channels after every pooling step. DarkNet-19 has 19 convolutional layers and 5 maximum pooling layers. The architecture of DarkNet-18 is shown in Table 3.

Table 3 The architecture of the DarkNet-19 CNN.

Layer Name	Number of filters	Size / Stride	Output
Convolutional	32	3×3	224×224
Maxpool	-	$2 \times 2 / 2$	112×112
Convolutional	64	3×3	112×112
Maxpool	-	$2 \times 2 / 2$	56×56
Convolutional	128	3×3	56×56
Convolutional	64	1×1	56×56
Convolutional	128	3×3	56×56
Maxpool	-	$2 \times 2 / 2$	28×28
Convolutional	256	3×3	28×28
Convolutional	128	1×1	28×28
Convolutional	256	3×3	28×28
Maxpool	-	$2 \times 2 / 2$	14×14
Convolutional	512	3×3	14×14
Convolutional	256	1×1	14×14
Convolutional	512	3×3	14×14
Convolutional	256	1×1	14×14
Convolutional	512	3×3	14×14
Maxpool	-	$2 \times 2 / 2$	7×7
Convolutional	1024	3×3	7×7
Convolutional	512	1×1	7×7
Convolutional	1024	3×3	7×7
Convolutional	512	1×1	7×7
Convolutional	1024	3×3	7×7
Convolutional	1000	1×1 Global	$7 \times 7 \times 2$
Avgpool			
Softmax			

SqueezeNet

SqueezeNet has 26 convolutional layers. The building block of SqueezeNet is called the fire module, which consists of two layers: a squeeze layer and an expand layer. The squeeze layer decreases the size of the feature map, while the [expandexpanded](#) layer increases it again. A SqueezeNet stacks a bunch of these fire modules and a few pooling layers [63]. The architecture of SqueezeNet and fire module is shown in Figure 2.



(a)

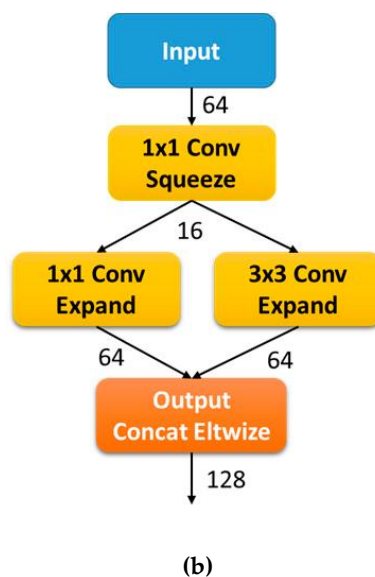


Figure 2 (a) SqueezeNet CNN architecture, (b) fire module of SqueezeNet

2.3. Grey level Co-occurrence Matrix

Co-occurrence distribution, also known as the gray-level co-occurrence matrix (GLCM), is a statistical analysis approach of the second order. It is a technique for texture analysis that has a variety of uses, most notably in the study of medical images [64–70]. It analyses the spatial relationships between pixels and quantifies the frequency with which a set of pixels appear together in an image at a certain distance and direction [71]. In other words, GLCM is used to specify the distribution of co-occurring pixel values (grayscale values) over an image at a specific offset [72]. In GLCM, a co-occurrence matrix is created by comparing the pixel values of adjacent pixels [73]. The total number of rows and columns equals the total number of pixel brightness values (gray level).

2.4. Proposed Auto-MyIn

This study proposes an automated tool called Auto-MyIn for diagnosing MI from DE-MRI images. The main aim of the study is to show that training CNNs with the textural information of the GLCM images is superior to using only the spatial information obtained from the original DE-MRI images. Furthermore, the study aims to investigate if fusing deep features from multiple CNNs trained using images generated with multi-levels of GLCM is capable of boosting the performance of Auto-MyIn. Moreover, it seeks to perform diagnosis without the need for segmentation steps or using clinical [data](#), which increases the complexity of the system. To achieve these goals Auto-MyIn utilizes the GLCM method with multi gray levels and three CNNs including ResNet-18, DarkNet-19, and SqueezeNet. Auto-MyIn consists of four steps which are DE-MRI image preprocessing and GLCM image generation, CNNs Training and feature extraction, feature fusion, and classification. In the DE-MRI image preprocessing and GLCM image generation step, the dimension of images is altered and augmented. [Furthermore](#), the GLCM method is applied to these images with several gray levels. Afterward, three [pre-trained](#) CNNs are constructed and retrained either with the original DE-MRI images or the GLCM images. Next, deep features are extracted from these CNNs and then fused in two phases. Finally, these deep features are used to train several SVM classifiers. Figure 3 shows the block diagram of the proposed Auto-MyIn.

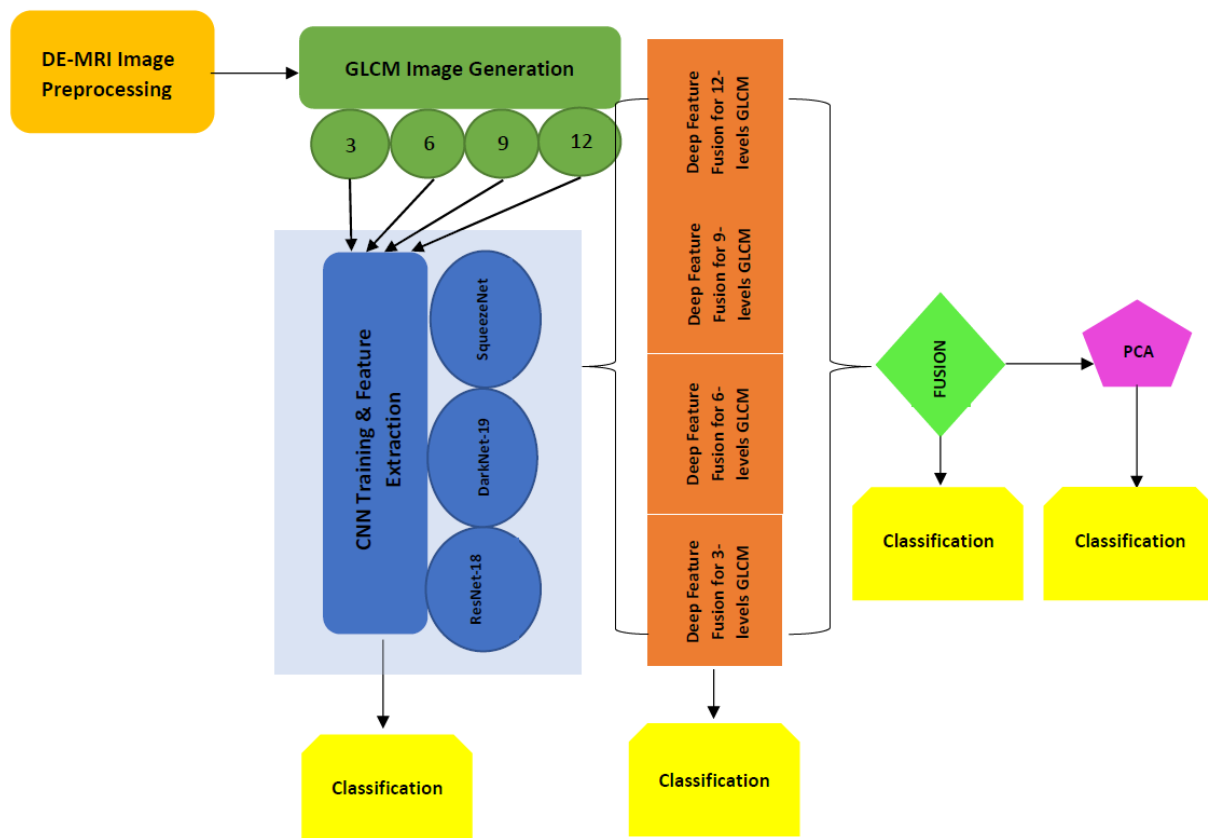


Figure 3. Block diagram of the proposed Auto-MyIn.

2.4.1. DE-MRI Image Preprocessing and GLCM Image Generation

In this step, the DE-MRI images are resized to be equal to the size of the input layer of the three CNNs which are $224 \times 224 \times 3$ for ResNet-18 and SqueezeNet, and $226 \times 226 \times 3$ for DarkNet-19. This step is done to allow the three CNNs to be able to start the training process. Then, these images are divided into training and testing data with a ratio of 70%-30%. The number of images used to train the CNN is [smallsmall](#), which may lead to overfitting and lower the training performance; therefore, augmentation is essential. Augmentation is a group of techniques that are used for modifying the current data to produce additional data for the model training procedure. In other words, it is the act of artificially increasing the dataset that can be used to train a deep learning model. This means that augmentation is capable of boosting the amount of training images to enhance the training performance and prevent overfitting [74]. The augmentation techniques applied are translation in X and Y directions where the translation distance range is chosen at random from within the range $(-30,30)$. [AlsoMoreover](#), scaling in X and Y directions is done with a scale chosen randomly within the range $(0.9,1.1)$.

Images of the dataset are then analyzed using the GLCM method. GLCM characterizes the texture of an image. This is accomplished by examining the spatial relationships between grey levels featured in an image and calculating the frequency with which a collection of grey levels appears together in an image [atfrom](#) a specific direction. The common orientations utilized in the literature are $(0, 45, 90, \text{ and } 135)$, therefore these directions are used in this study. The distance between the pixel of interest and its neighbor is $[0 \ 1; -1 \ 1; -1 \ 0; -1 \ -1]$, which is equivalent to the angles $(0,45,90,135)$. Afterwards, scaled images are generated from the GLCM with different number of grey levels including 3,6,9, and 12. These images represent texture information and are used as inputs to train the deep learning models of the Auto-MyIn instead of the original MRI images. Figure 4 shows samples of the original images and scaled images [efwith](#) reduced number of intensity values and different grey levels.

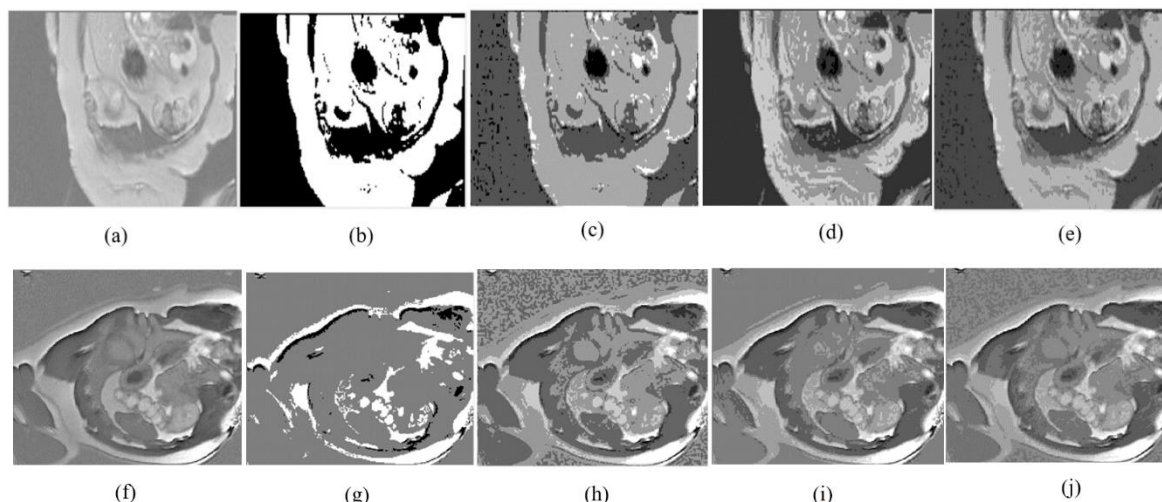


Figure 4. Samples of the scaled images with reduced number of intensity values (only 8) and different grey levels; (a) Normal original MRI slice, (b) normal scaled image with 3 grey levels, (c) normal scaled image with 6- grey levels, (d) normal scaled images with 9- grey levels, and (e) normal scaled images with 12-1 grey levels, (f) Pathology original MRI slice, (g) pathology scaled images with 3- levels GLCM image, (h) pathology scaled images with 6- grey levels, (i) pathology scaled images with 9- grey levels, and (j) pathology scaled images with 12- grey levels.

2.4.2. CNNs Training and Feature Extraction

This step represents the use of three ~~pre-trained~~ pretrained CNNs involving ResNet-18, DarkNet-19, and SqueezeNet constructed with transfer learning (TL) [75]. TL is a process widely used ~~within~~ deep learning models. TL is commonly utilized to benefit from the information gained while training a CNN with a large dataset to resolve a similar classification issue having few training images. This CNN learned with TL is called a ~~pre-trained~~ pretrained CNN. Initially, before retraining the pre-trained CNNs, TL is employed to modify the CNNs output layer to 2 (equal to the number of classes in the Emidec dataset) so that the CNNs can be capable of solving the current classification problem of Emidec dataset. Afterward, several CNNs' parameters are ~~adjusted~~ adjusted, which will be mentioned later. Then, these CNNs are retrained with either the original DE-MRI images of Emidec dataset or the scaled images generated with GLCM in the previous step. CNNs can be either used to perform end-to-end classification or as a feature extractor. In this study, the ~~pre-trained~~ pretrained CNNs are used as feature extractors. To extract deep features from these networks, after the retraining procedure of the CNNs is finished, TL is used again to extract deep features from the last average pooling layer of each CNN. The length of these deep features extracted from ResNet-18, DarkNet-19, and SqueezeNet is 512, 2, and 2, respectively.

2.4.3. Feature Fusion

This step represents the fusion of deep features obtained in the previous step. The fusion step is accomplished in two stages. In stage I, after extracting deep features from the three CNNs trained with the scaled images generated using GLCM with four different grey levels, the deep features obtained from each grey level of the three CNN are concatenated to form a feature vector of length 516. To reduce the dimension of these fused features, all deep features extracted from the three CNNs trained with scaled images of the four gray levels of GLCM images are fused using principal component analysis (PCA) in the second fusion stage [76]. PCA is a mathematical technique that reduces a large number of associated variables into a smaller set of variables known as principal components using advanced mathematical principles. In PCA, a dataset's integral projection onto a subspace produced by a system of orthogonal axes is used to store the information in a set of data with reduced dimensions. The significant features are determined with low information loss by using the reduced dimensions of computational content [77]. It performs a covariance analysis among

features. in other words, the PCA method lowers the number of features into new reduced features known as principal components. Such components reveal the variance among the original features.

2.4.4. Classification

This step corresponds to the classification procedure using several SVM classifiers of different kernels including linear, cubic, quadratic, median [gaussianGaussian](#), and cubic [gaussianGaussian](#). SVM is a well-known robust classifier. It is regarded as one of the most well-known techniques for classifying patterns and images [78]. Because it uses a kernel function to map the feature space into a new domain that can effectively differentiate between classes of a dataset, it performs well with huge dimension spaces and with multi-class. Due to its large dimension, it is frequently utilized [withto](#) DL features acquired from [CNNsCNNs](#), CNNs [52,53,78–84]. Therefore, it was employed in this study. 5-fold cross-validation is employed to validate the diagnostic performance of Auto-MyIn. The classification step of Auto-MyIn is made through three experiments. In experiment I, an end-to-end deep learning classification is [achievedachieved](#), where [the-threethree](#) pre-trained CNNs are trained [withon](#) scaled images of different grey levels generated using GLCM. Whereas in experiment II, for each grey level, deep features extracted from each CNN are concatenated and used to train the SVMs. Finally, in experiment III, all deep features from the four gray levels for the three CNNs are fused using PCA and used to train the SVM classifiers. An ablation study is performed in this experiment to show the effect of varying the number of principal components [withon](#) accuracy.

3. Setting of Experiments

3.1. Parameters Adjustment

The three CNNs are trained using the stochastic gradient with momentum after altering some parameters. These parameters include initial learning rate, number of epochs, minibatch size, and L2 regularization. The initial learning rate was adjusted to 0.00001, the number of epochs to 30, the minibatch size to 30, and L2 regularization to 0.0005. Other parameters were kept unaltered.

The specifications of the device used to perform the experiments are AMD Ryzen 7 5800H processor and NVIDIA GeForce RTX 3060, Windows 10, 64 bit with 16 GB of random-access memory (RAM). Additionally, we verified all the experiments with MATLAB R2021b software with the following libraries: the parallel computing toolbox, the deep learning toolbox, the [statisticsstatistics](#), and machine learning toolbox.

3.2. Evaluation Measures

Numerous measures are employed to assess the performance of the proposed Auto-MyIn. Such measures include the classification accuracy (CA), Matthew correlation coefficient (MCC), sensitivity, diagnostic odds ratio (DOR), specificity, Precision, and receiver operating characteristic (ROC) analysis. The following formulas (1-7) are used to calculate these measures.

$$CA = \frac{TP+TN}{TN+FP+FN+TP} \quad (1)$$

$$Sensitivity = \frac{TP}{TP+FN} \quad (2)$$

$$Specificity = \frac{TN}{TN+FP} \quad (3)$$

$$Precision = \frac{TP}{TP + FP} \quad (4)$$

$$MCC = \frac{TP \times TN - FP \times FN}{\sqrt{(TP + FP)(TP + FN)(TN + FP)(TN + FN)}} \quad (5)$$

$$DOR = \frac{TP \times TN}{FP \times FN} \quad (6)$$

$$F1 - Score = \frac{2 \times TP}{(2 \times TP) + FP + FN} \quad (7)$$

Where, Where TN is the true negative, which is the summation of negative class cases that are properly classified. TP is the true positive, which is the summation of positive class cases that are precisely diagnosed. FP is the false positive which is the amount of negative class cases that are wrongly recognized as positive class and FN is the false negative, which is the amount of positive class cases that are mistakenly recognized as negative class

3. Results

3.1. Results of Experiment I

The results of end-to-end deep learning classification using the three CNNs involving ResNet-18, DarkNet-19, and SqueezeNet are illustrated in this section. Table 4 shows the end-to-end deep learning classification results using ResNet-18, DarkNet-19, and SqueezeNet. These CNNs are trained individually with GLCM images of four gray levels. The table shows that the classification accuracy varies from 69.34% to 79.72%, the sensitivity ranges between 0.651 to 0.884, the specificity ranges (0.582, 0.691), the precision range (0.358, 0.815), F1-score ranges (0.49, 0.724), MCC ranges (0.274, 0.54), and DOR ranges (3.825, 16.828). Table 4 indicates that the highest accuracy is attained using ResNet-18 trained with GLCM images of 9 grey levels, whereas the worst performance is attained using ResNet-18 trained with GLCM images of 3 grey levels. The training process of the three CNN results obtained on Table 4 is shown in the supplementary material Figures S1-S3.

Table 4 End-to-end deep learning classification results using ResNet-18, DarkNet-19, and SqueezeNet trained individually with GLCM images of four gray levels.

CNN Architectures	Accuracy	Sensitivity	Specificity	Precision	F1-score	MCC	DOR
3-levels GLCM							
ResNet-18	0.6934	0.803	0.655	0.543	0.648	0.433	7.69
DarkNet-19	0.7075	0.703	0.652	0.6	0.648	0.351	4.418
SqueezeNet	0.7311	0.772	0.582	0.358	0.49	0.299	4.704
6-levels GLCM							
ResNet-18	0.7406	0.707	0.599	0.458	0.556	0.286	3.588
DarkNet-19	0.7547	0.714	0.662	0.615	0.661	0.372	4.869
SqueezeNet	0.7406	0.731	0.674	0.629	0.677	0.401	5.591
9-levels GLCM							
ResNet-18	0.7972	0.884	0.691	0.586	0.705	0.54	16.828
DarkNet-19	0.7406	0.747	0.595	0.415	0.534	0.306	4.317

SqueezeNet	0.7358	0.732	0.668	0.615	0.669	0.394	5.474
12-levels GLCM							
ResNet-18	0.7358	0.651	0.753	0.815	0.724	0.391	5.659
DarkNet-19	0.7453	0.736	0.58	0.372	0.495	0.274	3.825
SqueezeNet	0.7217	0.675	0.659	0.643	0.659	0.334	4.01

3.2. Results of Experiment II

This section illustrates the results of experiment II, where for each grey level, deep features extracted from the three CNNs trained with images generated from each grey level are concatenated. These features are used to feed SVM classifiers with different kernels. The classification accuracy achieved using these classifiers are shown in Figure 5. Figure 5 shows that for each level of GLCM images, the fusion of deep features has increased the classification accuracy compared to that indicated in Table 2. Furthermore, as indicated in Figure 4, the highest accuracy for the 5 kernels is attained with fused deep features of 9 levels of GLCM images except for cubic SVM, the highest accuracy is attained with fused deep features of 3 levels of GLCM images. Figure 2 also demonstrates that the maximum accuracy of 96.9% is reached using cubic SVM trained with fused deep features of 3 levels of GLCM followed by 96.3% attained using the cubic SVM fed with fused deep features of the 9 levels of GLCM images. The lowest accuracies of 88.7%, 90.4%, and 87.1% are achieved using the coarse gaussian SVM classifier trained with the fused deep features of the 3, 6, and 12 levels of GLCM images respectively.

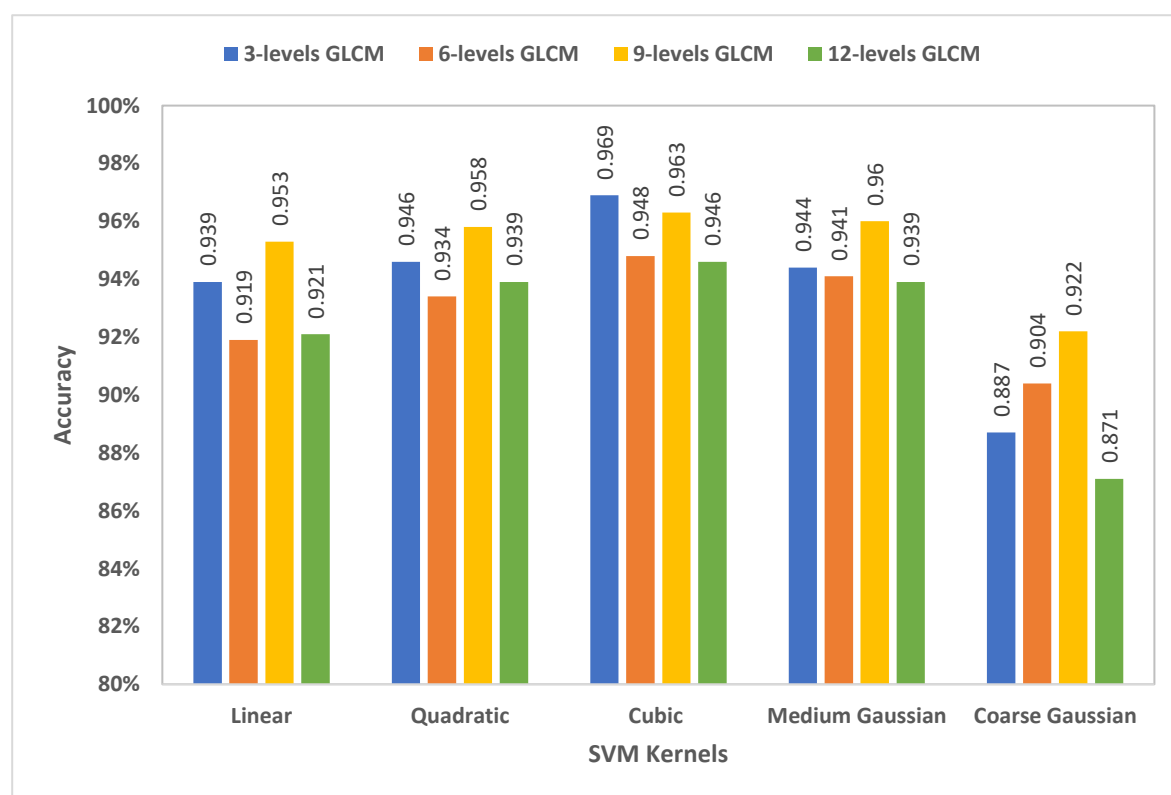


Figure 5. Classification accuracies of several SVM classifiers trained with the fused deep features of each GLCM level.

Figure 5 demonstrated that cubic SVM attained the highest accuracy compared to the other SVM classifiers. Therefore, other performance metrics are calculated for this classifier and shown in Table

5. Table 5 indicates that the performance of the cubic SVM classifier trained with the fused deep features of the three CNNs of 9 levels of GLCM is 0.983, 0.943, 0.94, 0.961, 0.923, and 864.3 for the sensitivity, specificity, precision, F1-score, MCC, and DOR, respectively. In addition, the sensitivity, specificity, precision, F1-score, MCC, and DOR using the fused deep features of the three CNNs trained with 3 levels of GLCM images are 0.981, 0.947, 0.945, 0.963, 0.927, and 873.924, respectively. The ROC curve of the cubic SVM classifier trained with the fused deep features of the three CNNs constructed with GLCM images having 9 grey levels is shown in Figure 6. Figure 6 shows that the AUC is 0.99.

Table 5 Performance metrics of the cubic SVM classifier trained with the fused deep features of the three CNNs constructed with GLCM images of different grey levels.

GLCM Levels	Accuracy (std)	Sensitivity (std)	Specificity (std)	Precision (std)	F1 score (std)	MCC (std)	DOR (std)
3-levels	0.969 (0.001)	0.981 (0.001)	0.947 (0.003)	0.945 (0.003)	0.963 (0.002)	0.927 (0.003)	873.924 (41.747)
6-levels	0.95 (0.002)	0.971 (0.003)	0.911 (0.002)	0.905 (0.003)	0.937 (0.002)	0.88 (0.003)	333.261 (28.835)
9-levels	0.963 (0.002)	0.983 (0.003)	0.943 (0.002)	0.94 (0.002)	0.961 (0.002)	0.923 (0.004)	864.3 (106.076)
12-levels	0.946 (0.001)	0.957 (0.002)	0.926 (0.002)	0.922 (0.002)	0.94 (0.001)	0.881 (0.002)	267.787 (7.061)

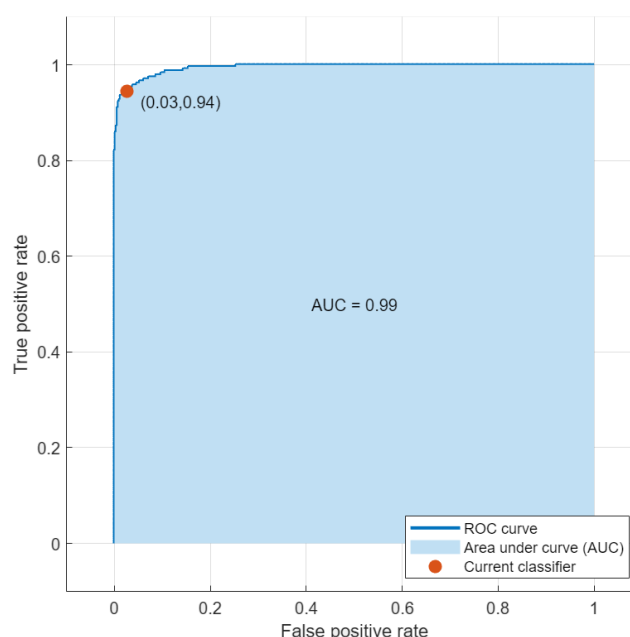


Figure 6. ROC curve of the cubic SVM classifier trained with the fused deep features of the three CNNs constructed with GLCM images having 9 grey levels.

3.3. Results of Experiment III

In this experiment, all deep features extracted from the three CNNs trained with the 4 levels of GLCM are fused all together using PCA. Figure 5 of experiment II indicated that the highest performance is achieved using the cubic SVM classifier. Therefore, it is used in experiment III. An ablation study is performed to show the effect of varying the number of principal components on classification accuracy. Figure 7 shows the results of this ablation study. Figure 7 indicates that the highest accuracy of 0.984 is attained using 50 components, thereafter the classification accuracy decreases.

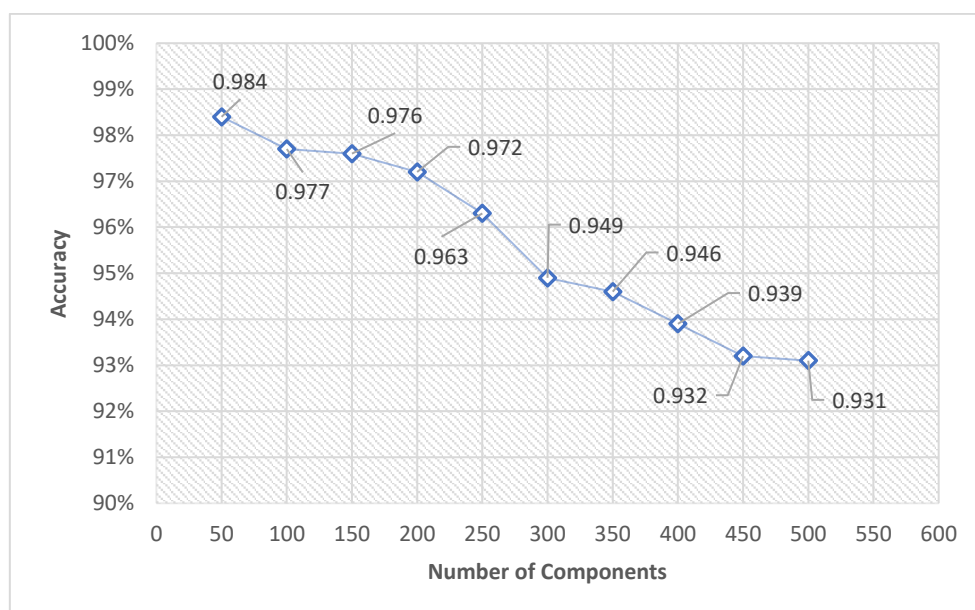


Figure 7. The classification accuracies of the cubic SVM classifier versus the number of principal components.

4. Discussions

The paper proposes an automated diagnostic tool called Auto-MyIn for diagnosing MI through an ensemble of CNNs. Textural information obtained from medical scans is helpful in clinical decision-making and uncovers important information to improve the diagnostic procedure of diseases and abnormalities. In textural analysis techniques, GLCM is extensively used in the medical and health fields. This method usually increases the performance of the diagnosis processes [27,85]. Thus, rather than using the original DE-MRI images, Auto-MyIn applied GLCM textural analysis method to obtain textural information from these images. Auto-MyIn applies the GLCM method with four grey levels on images. Then, the output of these grey levels of GLCM is used as images to feed three lightweight CNNs including ResNet-18, DarkNet 19, and SqueezeNet.

The classification process of Auto-MyIn is accomplished through experiments. Experiment I represents the end-to-end DL classification done by retraining the ~~pre-trained~~ pretrained CNNs with the levels of GLCM images. Experiment II corresponds to training several SVM classifiers with the fused deep features of each grey GLCM level extracted from the three CNNs trained with each grey level of GLCM images. In experiment III, all deep features of the four GLCM levels extracted from the three CNNs trained with each grey level of GLCM images are fused all together and used to feed the classifier. The peak accuracy attained in each experiment is shown in Figure 8. The accuracy achieved in experiment II (96.9%) is higher than that obtained in experiment I (79.72%). This means that fusing ~~deep~~ the deep features of each grey level of GLCM images can boost the diagnostic performance. In addition, the classification accuracy is further increased in experiment III to 98.4%, which indicates that fusing ~~deep~~ the deep features of the four grey levels extracted from the three CNNs trained with the four grey levels of GLCM images using PCA can further improve the diagnostic accuracy. note that the number of principal components is 50 which is much lower than the 516 features used in experiment II. This means that experiment III has lowered the complexity and computational load of the classification process.

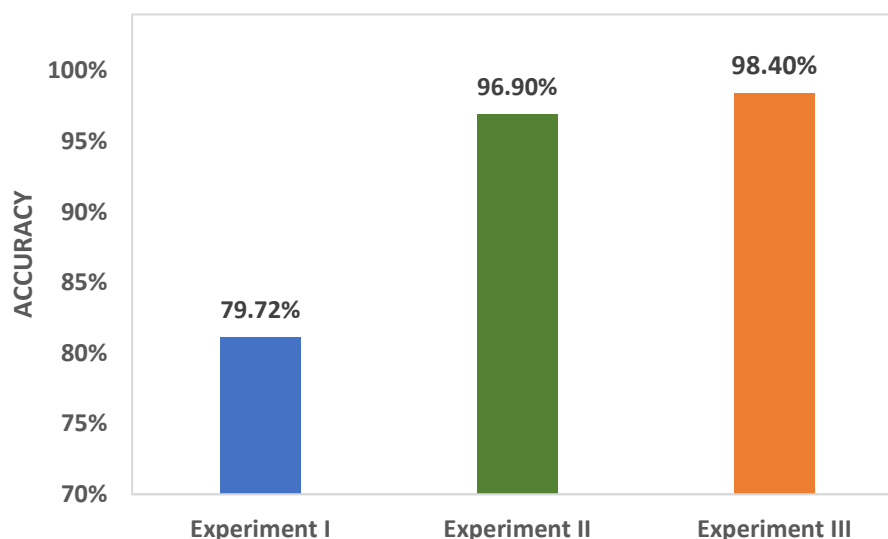


Figure 8. The peak classification accuracies attained in the three experiments.

The results of experiment III of Auto-MyIn are compared with the results attained by fusing deep features obtained from the three CNNs trained with the original DE-MRI images and shown in Table 6. Table 6 proves that fusing deep features of the four levels of GLCM images is superior to that of fusing deep features obtained from the original images. This is obvious as the accuracy, sensitivity, specificity, precision, F1-score, MCC, and DOR are 0.984, 0.992, 0.968, 0.967, 0.98, 0.96, and 3571.687 which are greater than those obtained using deep feature fusion of the original images (accuracy (0.973), sensitivity (0.983), specificity (0.955), precision (0.953), F1-score (0.968), MCC (0.937), and DOR (122.823)). As indicated by the studies [86–88], for a medical diagnostic tool to be reliable, it should achieve specificity and precision greater than 0.95, sensitivity more than 0.8, and a DOR that exceeds 100. The results of Auto-MyIn prove that it is a reliable tool, thus it can be used to facilitate the clinical decision-making process.

Table 6 Performance metrics comparison between those obtained using experiment III of Auto-MyIn and those achieved by fusing deep features extracted from the three CNNs trained with the original images.

Methods	Accuracy (std)	Sensitivity (std)	Specificity (std)	Precision (std)	F1 score (std)	MCC (std)	DOR (std)
Fusion of Deep Features (Original Images)	0.973 (0.001)	0.983 (0)	0.955 (0.009)	0.953 (0.009)	0.968 (0.005)	0.937 (0.009)	1222.823 (398.598)
Auto-MyIn (Experiment III)	0.984 (0.001)	0.992 (0.001)	0.968 (0.002)	0.967 (0.002)	0.98 (0.001)	0.96 (0.002)	3571.687 (153.774)

4.1. Comparison with Other Related Studies

The results of experiment III of Auto-MyIn are also compared with those of related studies based on the Emidec dataset and shown in Table 7. The table proves the competing ability of Auto-MyIn compared to other methods. This is obvious as the performance metrics attained using Auto-MyIn are higher than all studies except for [43] it has slightly lower sensitivity and precision but higher accuracy and specificity. Note that all previous studies used a segmentation step before the classification [process](#), which increases the complexity and computational cost of the system.

However, Auto-MyIn did not utilize a segmentation procedure and attained a competing performance. ~~Also~~Moreover, the majority of previous studies merged clinical data with DE-MRI images to perform ~~classification~~classification, which adds further computation load to the classification process. Nevertheless, Auto-MyIn produced superior performance without the need for this extra step.

Table 7 Performance metrics comparison between Auto-MyIn and those achieved by other related studies based on the Emidec dataset.

Studies	Accuracy	Sensitivity	Specificity	Precision
[41]	0.620	0.727	0.412	0.706
[42]	0.760	0.727	0.823	0.889
[89]	0.820	0.788	0.882	0.929
[40]	0.820	0.879	0.706	0.853
[39]	0.920	0.909	0.882	0.929
[43]	0.980	1.000	0.944	0.969
Auto-MyIn	0.984	0.992	0.968	0.967

4.2. Limitations

Despite the promising results achieved, this study suffers from numerous limitations. The first is that small training/validation samples which are not sufficient for deep learning of a ~~huge~~large number of hyperparameters. Additionally, the study did not consider any class imbalance method to deal with the imbalanced dataset. Besides, ~~optimization~~the optimization methods for selecting deep learning hyperparameters were not studied. Moreover, this study did not take into account the uncertainty of the input dataset. Noise existing in actual MRI scans could probably lower the diagnostic accuracy and this problem is not examined. The study does not investigate the problem, which is considered one of the limitations of the Auto-MyIn. Even though deep learning techniques have recently been successful in automating medical image processing and analysis tasks, the medical community still has doubts about their acceptability because their decision-making process isn't particularly transparent. Because of how opaquely they learn features, it is challenging to explain deep models' behavior and take advantage of any potential bottlenecks. Consequently, it is vital to determine if these deep features are associated with clinical features and whether their decision-making may be supported by traditional medical knowledge. One of the limitations of this study is not conducting a ~~correlation~~the correlation analysis to determine correlation among deep learned features and clinical observations in myocardial ~~infraction~~infarction. Future work will address this point by performing a correlation study to investigate associations between deep features and ~~the clinical~~clinical observations for myocardial infarction diagnosis

5. Conclusions

This study proposed an automated diagnostic tool, namely ~~Auto-MyIn~~Auto-MyIn, for diagnosing MI through multiple lightweight CNNs. Instead of using spatial information of the original DE-MRI to train the multiple CNNs, Auto-MyIn utilized the textural-based information to train these CNNs. this is done by applying the GLCM method with four different grey levels to DE-MRI, and then using the multiple GLCM images generated from the four grey levels to train these CNNs individually. The classification step of Auto-MyIn was executed via three experiments. First, an end-to-end DL procedure is done where the CNNs are used to perform classification. Next, in experiment II, deep features are extracted using TL, and then deep features of each grey level extracted from the three CNNs are fused and used to train several SVM classifiers. ~~finally~~Finally, in experiment III, all these deep features of the four grey levels of GLCM were fused all together using

PCA and fed to a cubic SVM classifier. The results of experiment II indicated that combining deep features of every GLCM grey level extracted with TL from the three CNNs is better than the end-to-end DL classification of experiment I. Furthermore, the results of experiment III showed that fusing ~~deep~~^{the deep} features of the four grey levels of GLCM using PCA has further enhancement in the diagnostic accuracy with a lower number of features which lowered the classification complexity and time. The results of experiment III of Auto-MyIn were compared with the results of the fusion of textural-based deep features obtained from the same CNNs but trained ~~with~~^{on} the original DE-MRI scans. This comparison proved that fusing textural information is superior to using the spatial information of the original DE-MRI images. In order to validate the competing ability of Auto-MyIn, its performance was compared with related studies based on the Emidec dataset. The comparison verified the competitiveness of Auto-MyIn. The key privilege of Auto-MyIn is that ~~outperformed~~^{outperforming} the performance of other related methods without the need for a segmentation process or adding further clinical ~~data~~^{data}, thus lowering the complexity and computational load of the system. The results of Auto-MyIn indicated that it is a reliable tool, therefore, it can be employed in a clinical setting to facilitate the diagnostic procedure. Future work will consider more textural analysis approaches. More deep learning models will be employed.

List of Abbreviations

AI	Artificial Intelligence
ANN	Artificial Neural Network
CA	Classification Accuracy
CNN	Convolutional Neural Networks
CV	Cardiovascular Diseases
DE-MRI	Delayed-Enhancement Magnetic Resonance
DOR	Diagnostic Odds Ratio
EF	Ejection Fraction
FN	False Negative
FP	False Positive
GLCM	Grey Level Covariance Matrix
MCC	Matthew Correlation Coefficient
MI	Myocardial Infarction
MRI	Magnetic Resonance Imaging
PCA	Principal Component Analysis
ROC	Receiver Operating Characteristic
ROI	Region of Interest
SVM	Support Vector Machine
TL	Transfer Learning
TN	True Negative
TP	True Positive
YOLO	You Only Look Once

Funding: This research received no external funding.

Conflicts of Interest: The authors declare no conflict of interest.

Data Availability Statement: The dataset used in this study can be found at <http://emidec.com/dataset>

References

1. Chang, Y.; Jung, C. Automatic Cardiac MRI Segmentation and Permutation-Invariant Pathology Classification Using Deep Neural Networks and Point Clouds. *Neurocomputing* **2020**, *418*, 270–279.
2. Romaguera, L.V.; Costa, M.G.F.; Romero, F.P.; Costa Filho, C.F.F. Left Ventricle Segmentation in Cardiac MRI Images Using Fully Convolutional Neural Networks. In Proceedings of the Medical Imaging 2017: Computer-Aided Diagnosis; International Society for Optics and Photonics, 2017; Vol. 10134, p. 101342Z.
3. Lalande, A.; Chen, Z.; Decourselle, T.; Qayyum, A.; Pommier, T.; Lorgis, L.; de la Rosa, E.; Cochet, A.; Cottin, Y.; Ginhac, D. Emidec: A Database Usable for the Automatic Evaluation of Myocardial Infarction from Delayed-Enhancement Cardiac Mri. *Data* **2020**, *5*, 89.
4. Sharma, L.D.; Sunkaria, R.K. Inferior Myocardial Infarction Detection Using Stationary Wavelet Transform and Machine Learning Approach. *Signal, Image and Video Processing* **2018**, *12*, 199–206.
5. Michaud, K.; Basso, C.; d'Amati, G.; Giordano, C.; Kholová, I.; Preston, S.D.; Rizzo, S.; Sabatasso, S.; Sheppard, M.N.; Vink, A. Diagnosis of Myocardial Infarction at Autopsy: AECVP Reappraisal in the Light of the Current Clinical Classification. *Virchows Archiv* **2020**, *476*, 179–194.
6. Arevalo, H.J.; Vadakkumpadan, F.; Guallar, E.; Jebb, A.; Malamas, P.; Wu, K.C.; Trayanova, N.A. Arrhythmia Risk Stratification of Patients after Myocardial Infarction Using Personalized Heart Models. *Nature communications* **2016**, *7*, 1–8.
7. Bax, J.J.; Baumgartner, H.; Ceconi, C.; Dean, V.; Fagard, R.; Funck-Brentano, C.; Hasdai, D.; Hoes, A.; Kirchhof, P.; Knuuti, J. Third Universal Definition of Myocardial Infarction. *Journal of the American College of Cardiology* **2012**, *60*, 1581–1598.
8. Feng, K.; Pi, X.; Liu, H.; Sun, K. Myocardial Infarction Classification Based on Convolutional Neural Network and Recurrent Neural Network. *Applied Sciences* **2019**, *9*, 1879.
9. Mozaffarian, D.; Benjamin, E.J.; Go, A.S.; Arnett, D.K.; Blaha, M.J.; Cushman, M.; De Ferranti, S.; Després, J.-P.; Fullerton, H.J.; Howard, V.J. Executive Summary: Heart Disease and Stroke Statistics—2015 Update: A Report from the American Heart Association. *Circulation* **2015**, *131*, 434–441.
10. Reddy, K.S.; Yusuf, S. Emerging Epidemic of Cardiovascular Disease in Developing Countries. *Circulation* **1998**, *97*, 596–601.
11. Organization, W.H. *World Health Statistics 2015*; World Health Organization, 2015;
12. Jahmunah, V.; Ng, E.Y.K.; San, T.R.; Acharya, U.R. Automated Detection of Coronary Artery Disease, Myocardial Infarction and Congestive Heart Failure Using GaborCNN Model with ECG Signals. *Computers in biology and medicine* **2021**, *134*, 104457.
13. Merjulah, R.; Chandra, J. Classification of Myocardial Ischemia in Delayed Contrast Enhancement Using Machine Learning. In *Intelligent Data Analysis for Biomedical Applications*; Elsevier, 2019; pp. 209–235.
14. Xu, B.; Kocyigit, D.; Grimm, R.; Griffin, B.P.; Cheng, F. Applications of Artificial Intelligence in Multimodality Cardiovascular Imaging: A State-of-the-Art Review. *Progress in cardiovascular diseases* **2020**.

15. Mannil, M.; Eberhard, M.; von Spiczak, J.; Heindel, W.; Alkadhi, H.; Baessler, B. Artificial Intelligence and Texture Analysis in Cardiac Imaging. *Current Cardiology Reports* **2020**, *22*, 1–9.
16. Weinsaft, J.W.; Klem, I.; Judd, R.M. MRI for the Assessment of Myocardial Viability. *Magnetic resonance imaging clinics of North America* **2007**, *15*, 505–525.
17. Arai, A.E. The Cardiac Magnetic Resonance (CMR) Approach to Assessing Myocardial Viability. *Journal of Nuclear Cardiology* **2011**, *18*, 1095–1102.
18. Shehata, M.L.; Turkbey, E.B.; Vogel-Claussen, J.; Bluemke, D.A. Role of Cardiac Magnetic Resonance Imaging in Assessment of Nonischemic Cardiomyopathies. *Topics in Magnetic Resonance Imaging* **2008**, *19*, 43–57.
19. El Ogri, O.; Karmouni, H.; Sayyouri, M.; Qjidaa, H. 3D Image Recognition Using New Set of Fractional-Order Legendre Moments and Deep Neural Networks. *Signal Processing: Image Communication* **2021**, *98*, 116410.
20. Attallah, O. ECG-BiCoNet: An ECG-Based Pipeline for COVID-19 Diagnosis Using Bi-Layers of Deep Features Integration. *Computers in Biology and Medicine* **2022**, 105210.
21. Ragab, D.A.; Sharkas, M.; Attallah, O. Breast Cancer Diagnosis Using an Efficient CAD System Based on Multiple Classifiers. *Diagnostics* **2019**, *9*, 165.
22. Attallah, O.; Anwar, F.; Ghanem, N.M.; Ismail, M.A. Histo-CADx: Duo Cascaded Fusion Stages for Breast Cancer Diagnosis from Histopathological Images. *PeerJ Computer Science* **2021**, *7*, e493.
23. Attallah, O.; Karthikesalingam, A.; Holt, P.J.; Thompson, M.M.; Sayers, R.; Bown, M.J.; Choke, E.C.; Ma, X. Feature Selection through Validation and Un-Censoring of Endovascular Repair Survival Data for Predicting the Risk of Re-Intervention. *BMC medical informatics and decision making* **2017**, *17*, 115–133.
24. Attallah, O.; Karthikesalingam, A.; Holt, P.J.; Thompson, M.M.; Sayers, R.; Bown, M.J.; Choke, E.C.; Ma, X. Using Multiple Classifiers for Predicting the Risk of Endovascular Aortic Aneurysm Repair Re-Intervention through Hybrid Feature Selection. *Proceedings of the Institution of Mechanical Engineers, Part H: Journal of Engineering in Medicine* **2017**, *231*, 1048–1063.
25. Karthikesalingam, A.; Attallah, O.; Ma, X.; Bahia, S.S.; Thompson, L.; Vidal-Diez, A.; Choke, E.C.; Bown, M.J.; Sayers, R.D.; Thompson, M.M. An Artificial Neural Network Stratifies the Risks of Reintervention and Mortality after Endovascular Aneurysm Repair; a Retrospective Observational Study. *PloS one* **2015**, *10*, e0129024.
26. Attallah, O.; Ma, X. Bayesian Neural Network Approach for Determining the Risk of Re-Intervention after Endovascular Aortic Aneurysm Repair. *Proceedings of the Institution of Mechanical Engineers, Part H: Journal of Engineering in Medicine* **2014**, *228*, 857–866.
27. Attallah, O.; Sharkas, M.A.; Gadelkarim, H. Fetal Brain Abnormality Classification from MRI Images of Different Gestational Age. *Brain Sciences* **2019**, *9*, 231–252.
28. Attallah, O.; Abougharbia, J.; Tamazin, M.; Nasser, A.A. A BCI System Based on Motor Imagery for Assisting People with Motor Deficiencies in the Limbs. *Brain sciences* **2020**, *10*, 864–888.

29. Attallah, O. DIAROP: Automated Deep Learning-Based Diagnostic Tool for Retinopathy of Prematurity. *Diagnostics* **2021**, *11*, 2034.
30. Yum, B.; Adelsheimer, A.; Tafreshi, R.; Hagopian, R.; Kim, J. Clinical Implications of Machine Learning, Artificial Intelligence, and Radiomics in Cardiac Imaging. *Current Treatment Options in Cardiovascular Medicine* **2020**, *22*, 1–13.
31. Mathur, P.; Srivastava, S.; Xu, X.; Mehta, J.L. Artificial Intelligence, Machine Learning, and Cardiovascular Disease. *Clinical Medicine Insights: Cardiology* **2020**, *14*, 1179546820927404.
32. Martin-Isla, C.; Campello, V.M.; Izquierdo, C.; Raisi-Estabragh, Z.; Baeßler, B.; Petersen, S.E.; Lekadir, K. Image-Based Cardiac Diagnosis with Machine Learning: A Review. *Frontiers in Cardiovascular Medicine* **2020**, *7*, 1.
33. Larroza, A.; López-Lereu, M.P.; Monmeneu, J.V.; Gavara, J.; Chorro, F.J.; Bodí, V.; Moratal, D. Texture Analysis of Cardiac Cine Magnetic Resonance Imaging to Detect Nonviable Segments in Patients with Chronic Myocardial Infarction. *Medical physics* **2018**, *45*, 1471–1480.
34. Yang, F.; Yang, X.; Teo, S.K.; Lee, G.; Zhong, L.; San Tan, R.; Su, Y. Multi-Dimensional Proprio-Proximus Machine Learning for Assessment of Myocardial Infarction. *Computerized Medical Imaging and Graphics* **2018**, *70*, 63–72.
35. Khened, M.; Alex, V.; Krishnamurthi, G. Densely Connected Fully Convolutional Network for Short-Axis Cardiac Cine MR Image Segmentation and Heart Diagnosis Using Random Forest. In Proceedings of the International Workshop on Statistical Atlases and Computational Models of the Heart; Springer, 2017; pp. 140–151.
36. Isensee, F.; Jaeger, P.F.; Full, P.M.; Wolf, I.; Engelhardt, S.; Maier-Hein, K.H. Automatic Cardiac Disease Assessment on Cine-MRI via Time-Series Segmentation and Domain Specific Features. In Proceedings of the International workshop on statistical atlases and computational models of the heart; Springer, 2017; pp. 120–129.
37. Chen, M.; Fang, L.; Zhuang, Q.; Liu, H. Deep Learning Assessment of Myocardial Infarction from MR Image Sequences. *IEEE Access* **2019**, *7*, 5438–5446.
38. Xu, C.; Xu, L.; Zhang, H.; Zhang, Y.; Du, X.; Li, S. A Novel Machine-Learning Algorithm to Estimate the Position and Size of Myocardial Infarction for MRI Sequence. *Computing* **2019**, *101*, 653–665.
39. Shi12, J.; Chen, Z.; Couturier, R. Classification of Pathological Cases of Myocardial Infarction Using Convolutional Neural Network and Random Forest.
40. Lourenço, A.; Kerfoot, E.; Grigorescu, I.; Scannell, C.M.; Varela, M.; Correia, T.M. Automatic Myocardial Disease Prediction From Delayed-Enhancement Cardiac MRI and Clinical Information. *arXiv preprint arXiv:2010.08469* **2020**.
41. Sharma, R.; Eick, C.F.; Tsekos, N.V. SM2N2: A Stacked Architecture for Multimodal Data and Its Application to Myocardial Infarction Detection★.
42. Ivantsits, M.; Huellebrand, M.; Kelle, S.; Schönberg, S.; Kuehne, T.; Hennemuth, A. Deep-Learning-Based Myocardial Pathology Detection.
43. Brahim, K.; Arega, T.W.; Boucher, A.; Bricq, S.; Sakly, A.; Meriaudeau, F. An Improved 3D Deep Learning-Based Segmentation of Left Ventricular Myocardial

- Diseases from Delayed-Enhancement MRI with Inclusion and Classification Prior Information U-Net (ICPIU-Net). *Sensors* **2022**, *22*, 2084.
44. de la Rosa, E.; Sidibé, D.; Decourselle, T.; Leclercq, T.; Cochet, A.; Lalande, A. Myocardial Infarction Quantification from Late Gadolinium Enhancement MRI Using Top-Hat Transforms and Neural Networks. *Algorithms* **2021**, *14*, 249.
 45. Biswas, S.; Chatterjee, S.; Majee, A.; Sen, S.; Schwenker, F.; Sarkar, R. Prediction of Covid-19 from Chest Ct Images Using an Ensemble of Deep Learning Models. *Applied Sciences* **2021**, *11*, 7004.
 46. Zhou, T.; Lu, H.; Yang, Z.; Qiu, S.; Huo, B.; Dong, Y. The Ensemble Deep Learning Model for Novel COVID-19 on CT Images. *Applied Soft Computing* **2021**, *98*, 106885.
 47. Poirion, O.B.; Jing, Z.; Chaudhary, K.; Huang, S.; Garmire, L.X. DeepProg: An Ensemble of Deep-Learning and Machine-Learning Models for Prognosis Prediction Using Multi-Omics Data. *Genome medicine* **2021**, *13*, 1–15.
 48. Nadeem, S.; Tahir, M.A.; Naqvi, S.S.A.; Zaid, M. Ensemble of Texture and Deep Learning Features for Finding Abnormalities in the Gastro-Intestinal Tract. In Proceedings of the International Conference on Computational Collective Intelligence; Springer, 2018; pp. 469–478.
 49. Ali, H.; Sharif, M.; Yasmin, M.; Rehmani, M.H.; Riaz, F. A Survey of Feature Extraction and Fusion of Deep Learning for Detection of Abnormalities in Video Endoscopy of Gastrointestinal-Tract. *Artificial Intelligence Review* **2019**, 1–73.
 50. Amin, J.; Sharif, A.; Gul, N.; Anjum, M.A.; Nisar, M.W.; Azam, F.; Bukhari, S.A.C. Integrated Design of Deep Features Fusion for Localization and Classification of Skin Cancer. *Pattern Recognition Letters* **2020**, *131*, 63–70.
 51. Amrani, M.; Hammad, M.; Jiang, F.; Wang, K.; Amrani, A. Very Deep Feature Extraction and Fusion for Arrhythmias Detection. *Neural Comput & Applic* **2018**, *30*, 2047–2057, doi:10.1007/s00521-018-3616-9.
 52. Ragab, D.A.; Sharkas, M.; Marshall, S.; Ren, J. Breast Cancer Detection Using Deep Convolutional Neural Networks and Support Vector Machines. *PeerJ* **2019**, *7*, e6201.
 53. Ragab, D.A.; Attallah, O.; Sharkas, M.; Ren, J.; Marshall, S. A Framework for Breast Cancer Classification Using Multi-DCNNs. *Computers in Biology and Medicine* **2021**, *131*, 104245.
 54. Attallah, O.; Sharkas, M.A.; Gadelkarim, H. Deep Learning Techniques for Automatic Detection of Embryonic Neurodevelopmental Disorders. *Diagnostics* **2020**, *10*, 27–49.
 55. Litjens, G.; Kooi, T.; Bejnordi, B.E.; Setio, A.A.A.; Ciompi, F.; Ghafoorian, M.; Van Der Laak, J.A.; Van Ginneken, B.; Sánchez, C.I. A Survey on Deep Learning in Medical Image Analysis. *Medical image analysis* **2017**, *42*, 60–88.
 56. Liu, W.; Wang, Z.; Liu, X.; Zeng, N.; Liu, Y.; Alsaadi, F.E. A Survey of Deep Neural Network Architectures and Their Applications. *Neurocomputing* **2017**, *234*, 11–26.
 57. Alom, M.Z.; Taha, T.M.; Yakopcic, C.; Westberg, S.; Sidike, P.; Nasrin, M.S.; Hasan, M.; Van Essen, B.C.; Awwal, A.A.; Asari, V.K. A State-of-the-Art Survey on Deep Learning Theory and Architectures. *Electronics* **2019**, *8*, 292–357.

58. Bhuiyan, M.N.Q.; Shamsujjoha, M.; Ripon, S.H.; Proma, F.H.; Khan, F. Transfer Learning and Supervised Classifier Based Prediction Model for Breast Cancer. In *Big Data Analytics for Intelligent Healthcare Management*; Elsevier, 2019; pp. 59–86.
59. Byra, M.; Styczynski, G.; Szmigielski, C.; Kalinowski, P.; Michałowski, Ł.; Paluszkiewicz, R.; Ziarkiewicz-Wróblewska, B.; Zieniewicz, K.; Sobieraj, P.; Nowicki, A. Transfer Learning with Deep Convolutional Neural Network for Liver Steatosis Assessment in Ultrasound Images. *Int J CARS* **2018**, *13*, 1895–1903, doi:10.1007/s11548-018-1843-2.
60. Pan, S.J.; Yang, Q. A Survey on Transfer Learning. *IEEE Transactions on knowledge and data engineering* **2009**, *22*, 1345–1359.
61. Han, D.; Liu, Q.; Fan, W. A New Image Classification Method Using CNN Transfer Learning and Web Data Augmentation. *Expert Systems with Applications* **2018**, *95*, 43–56.
62. He, K.; Zhang, X.; Ren, S.; Sun, J. Deep Residual Learning for Image Recognition. In Proceedings of the Proceedings of the IEEE conference on computer vision and pattern recognition; IEEE, 2016; pp. 770–778.
63. Iandola, F.N.; Han, S.; Moskewicz, M.W.; Ashraf, K.; Dally, W.J.; Keutzer, K. SqueezeNet: AlexNet-Level Accuracy with 50x Fewer Parameters And< 0.5 MB Model Size. *arXiv preprint arXiv:1602.07360* **2016**.
64. Kumar, D. Feature Extraction and Selection of Kidney Ultrasound Images Using GLCM and PCA. *Procedia Computer Science* **2020**, *167*, 1722–1731.
65. Htay, T.T.; Maung, S.S. Early Stage Breast Cancer Detection System Using Glcm Feature Extraction and K-Nearest Neighbor (k-NN) on Mammography Image. In Proceedings of the 2018 18th International Symposium on Communications and Information Technologies (ISCIT); IEEE, 2018; pp. 171–175.
66. Kamalakannan, J.; Babu, M.R. Classification of Breast Abnormality Using Decision Tree Based on GLCM Features in Mammograms. *International Journal of Computer Aided Engineering and Technology* **2018**, *10*, 504–512.
67. Gurunathan, A.; Krishnan, B. A Hybrid CNN-GLCM Classifier For Detection And Grade Classification Of Brain Tumor. *Brain Imaging and Behavior* **2022**, *16*, 1410–1427.
68. Jehangir, B.; Nayak, S.R. GLCM Based LGBM Classification for COVID-19 Analysis Using Chest X-Ray Images. In Proceedings of the 2022 12th International Conference on Cloud Computing, Data Science & Engineering (Confluence); IEEE, 2022; pp. 477–481.
69. Althubiti, S.A.; Paul, S.; Mohanty, R.; Mohanty, S.N.; Alenezi, F.; Polat, K. Ensemble Learning Framework with GLCM Texture Extraction for Early Detection of Lung Cancer on CT Images. *Computational and Mathematical Methods in Medicine* **2022**, *2022*.
70. Napoleon, D.; Kalaiarasi, I. Classifying Lung Cancer as Benign and Malignant Nodule Using ANN of Back-Propagation Algorithm and GLCM Feature Extraction on Chest X-Ray Images. *Wireless Personal Communications* **2022**, *1–29*.
71. Nanni, L.; Brahnam, S.; Ghidoni, S.; Menegatti, E.; Barrier, T. Different Approaches for Extracting Information from the Co-Occurrence Matrix. *PloS one* **2013**, *8*, e83554.

- 770 72. Mishra, S.; Majhi, B.; Sa, P.K.; Sharma, L. Gray Level Co-Occurrence Matrix and
 771 Random Forest Based Acute Lymphoblastic Leukemia Detection. *Biomedical Signal*
 772 *Processing and Control* **2017**, *33*, 272–280.
- 773 73. Gebejes, A.; Huertas, R. Texture Characterization Based on Grey-Level Co-Occurrence
 774 Matrix. *Databases* **2013**, *9*, 375–378.
- 775 74. Shorten, C.; Khoshgoftaar, T.M. A Survey on Image Data Augmentation for Deep
 776 Learning. *Journal of Big Data* **2019**, *6*, 1–48.
- 777 75. Lu, J.; Behbood, V.; Hao, P.; Zuo, H.; Xue, S.; Zhang, G. Transfer Learning Using
 778 Computational Intelligence: A Survey. *Knowledge-Based Systems* **2015**, *80*, 14–23.
- 779 76. Abdi, H.; Williams, L.J. Principal Component Analysis. *Wiley interdisciplinary reviews:*
 780 *computational statistics* **2010**, *2*, 433–459.
- 781 77. Nandi, D.; Ashour, A.S.; Samanta, S.; Chakraborty, S.; Salem, M.A.; Dey, N. Principal
 782 Component Analysis in Medical Image Processing: A Study. *International Journal of*
 783 *Image Mining* **2015**, *1*, 65–86.
- 784 78. Thai, L.H.; Hai, T.S.; Thuy, N.T. Image Classification Using Support Vector Machine
 785 and Artificial Neural Network. *International Journal of Information Technology and*
 786 *Computer Science* **2012**, *4*, 32–38.
- 787 79. Leng, J.; Li, T.; Bai, G.; Dong, Q.; Dong, H. Cube-CNN-SVM: A Novel Hyperspectral
 788 Image Classification Method. In Proceedings of the 2016 IEEE 28th International
 789 Conference on Tools with Artificial Intelligence (ICTAI); IEEE, 2016; pp. 1027–1034.
- 790 80. Wu, H.; Huang, Q.; Wang, D.; Gao, L. A CNN-SVM Combined Model for Pattern
 791 Recognition of Knee Motion Using Mechanomyography Signals. *Journal of*
 792 *Electromyography and Kinesiology* **2018**, *42*, 136–142.
- 793 81. Attallah, O. A Computer-Aided Diagnostic Framework for Coronavirus Diagnosis Using
 794 Texture-Based Radiomics Images. *DIGITAL HEALTH* **2022**, *8*, 20552076221092544.
- 795 82. Ragab, D.A.; Sharkas, M.; Marshall, S.; Ren, J. Breast Cancer Detection Using Deep
 796 Convolutional Neural Networks and Support Vector Machines. *PeerJ* **2019**, *7*, e6201.
- 797 83. Sampaio, W.B.; Diniz, E.M.; Silva, A.C.; De Paiva, A.C.; Gattass, M. Detection of
 798 Masses in Mammogram Images Using CNN, Geostatistic Functions and SVM.
 799 *Computers in Biology and Medicine* **2011**, *41*, 653–664.
- 800 84. Attallah, O.; Zaghlool, S. AI-Based Pipeline for Classifying Pediatric Medulloblastoma
 801 Using Histopathological and Textural Images. *Life* **2022**, *12*, 232.
- 802 85. Nailon, W.H. Texture Analysis Methods for Medical Image Characterisation.
 803 *Biomedical Imaging* **2010**, doi:10.5772/8912.
- 804 86. Attallah, O. An Effective Mental Stress State Detection and Evaluation System Using
 805 Minimum Number of Frontal Brain Electrodes. *Diagnostics* **2020**, *10*, 292–327.
- 806 87. Colquhoun, D. An Investigation of the False Discovery Rate and the Misinterpretation
 807 of P-Values. *Royal Society open science* **2014**, *1*, 140216.
- 808 88. Ellis, P.D. *The Essential Guide to Effect Sizes: Statistical Power, Meta-Analysis, and the*
 809 *Interpretation of Research Results*; Cambridge University Press, 2010;
- 810 89. Girum, K.B.; Skandarani, Y.; Hussain, R.; Grayeli, A.B.; Créhange, G.; Lalande, A.
 811 Automatic Myocardial Infarction Evaluation from Delayed-Enhancement Cardiac MRI

812 Using Deep Convolutional Networks. In Proceedings of the International Workshop on
813 Statistical Atlases and Computational Models of the Heart; Springer, 2020; pp. 378–384.
814